Article type : Technical Paper

Intercomparison of Satellite Remote Sensing Based Flood Inundation Mapping Techniques

Dinuke Munasinghe, Sagy Cohen, Yu-Fen Huang, Yin-Phan Tsang, Jiaqi Zhang, and Zheng Fang

Graduate Student (**Munasinghe**) and Assistant Professor (**Cohen**), Department of Geography, University of Alabama, 513 University Boulevard, Tuscaloosa, Alabama 35487; Graduate Student (**Huang**) and Assistant Professor (**Tsang**), Department of Natural Resources and Environmental Management, University of Hawaii at Manoa, Honolulu, Hawaii 96822; and Graduate Student (**Zhang**) and Assistant Professor (**Fang**), Department of Civil and Environmental Engineering, University of Texas at Arlington, Arlington, Texas 76019 (E-Mail/Cohen: sagy.cohen@ua.edu).

Abstract: The objective of this study is to determine the accuracy of five different digital image processing techniques to map flood inundation extent with Landsat 8 - OLI satellite imagery. The May of 2016 flooding event in the Hempstead region of the Brazos River, TX, USA is used as a case study for this first comprehensive comparison of classification techniques of its kind. Five flood water classification techniques (*i.e.* supervised classification, unsupervised classification, delta cue change detection, normalized difference water index (NDWI), modified normalized difference water index (MNDWI)) were implemented to characterize flooded regions. To identify flood water obscured by cloud cover, a Digital Elevation Model (DEM) based approach was employed. Classified floods were compared using an Advance Fitness Index to a ‘reference flood map’ created based on manual digitization, as well as other data sources, using the same satellite image. Supervised classification yielded the highest accuracy of 86.4%, while unsupervised, MNDWI, and NDWI closely followed at 79.6%, 77.3% and 77.1%, respectively. Delta-cue change detection yielded the lowest accuracy with 70.1%. Thus, supervised classification is recommended for flood water classification and inundation map generation under these settings. The DEM based approach used to identify cloud-obscured flood water pixels was found reliable and easy to apply. It is therefore recommended for regions with relatively flat topography.

(**Key Terms:** Flooding; Remote Sensing; Inundation mapping; Geospatial Analysis; Image Classification.)

INTRODUCTION

Floods are one of the leading natural disasters which devastate agricultural crops and property, disrupt businesses, cause the loss of human lives and have huge impacts on national economies (Lakshmi, 2016). It is of concern that with the onset of climate change, flood intensities and frequencies will continue to threaten global livelihoods (Kahn *et al*., 2011). Thus, the current trend and future scenarios of flood risks demand accurate spatial and temporal information on the potential hazards and risks of floods. Precise knowledge of the spatial extent of inundated areas is essential both during the floods, when it is necessary to have an overall view of the phenomenon in order to plan immediate relief efforts, and for detecting deficiencies in existing food control mechanisms, which is vital for planning future mitigation activities. Only if the general public and first responders are provided with accurate information of the flood risk, and only if they are able to evaluate the risk, can they be expected to adequately respond to this threat. Implementing tools for near-real time estimation of flood magnitudes could allow better mitigation strategies by producing immediate data to scientists and decision makers. Although Floodplain mapping based on ground surveys and aerial observations provide an option, when the flooding is widespread and frequent, such methods are time-consuming, expensive and slow down the pace of assessing the impact of the flood on the economy and livelihood.

An alternative is to use satellite imagery, capable of providing synoptic views of flood dynamics. The use of remote sensing for flood mitigation has become popular over the past few decades thanks to significant improvement of geospatial technologies and data availability (e.g. Sanyal and Lu, 2004; Kahn *et al*., 2011). As technology is enhanced remote sensing data have emerged as a viable alternative or supplement to *in situ* observations due to their availability for ungauged regions. The advantages of using remotely sensed data in flood mapping are: almost a near-real time surveillance of flooding extent, the extensive spatial coverage of the data, the effectiveness and robustness of the flood mapping methods, and the relatively low cost for mapping a flood of large aerial extent.

The utility of satellite remote sensing has been proven in different domains. Flood spatial extent information obtained from orbital sensors are used to calibrate and evaluate hydraulic models when there is the lack of appropriate distributed validation and calibration data in an effort to potentially improve hydrologic prediction and flood management strategies in ungauged catchments (e.g. Horritt, 2000). Such results are in turn used to inform major decisions relating to planning of National Flood Insurance policies and generation of flood hazard maps (Federal Emergency Management Agency flood map service center, 2017. Accessed January 2017, https://msc.fema.gov/portal). Flood zone risk assessments on personal and state properties, and decisions with regards to flood insurance premiums solely depend on these flood maps. Earth observations also provide objective information about the spatiotemporal evolution of floods occurring in the same region which has resulted in characterization of flood extent over time (Islam *et al*., 2010; Huang *et al*., 2014). Flooding is an essential factor for the well-being of floral and faunal communities in river corridors, and these observations provide supplementary information about their living conditions which are closely related to flood inundation characteristics such as extent and frequency (Robertson *et al.*, 2001). The said values, thus, has led to the build-up of the demand for near-real time monitoring of flood disasters and are addressing the operational requirements of decision support systems used by policy makers, emergency managers and responders from international and federal to regional, state and local jurisdictions. (Joyce *et al*., 2009)

In recent decades, remotely sensed imagery has been used in many studies to map inundated areas over regions characterized by very different conditions in climate, morphology and land use (Schultz, 1988; Bates *et al.*, 1997; see Smith, 1997). Much of the pioneering work on the remote sensing of floods was accomplished using the Multi-Spectral Scanner (MSS) sensor on ERTS-1 (the first Earth Resources Technology Satellite, later renamed Landsat-1), launched in

July 1972. With a spatial resolution of about 80 m, MSS data were used to map the extent of flooding in Iowa (Hallberg *et al*., 1973; Rango and Salomonson, 1974; see Smith, 1997), Arizona (Morrison and Cooley, 1973; see Smith, 1997), Virginia (Rango and Salomonson, 1974; see Smith, 1997) and along the Mississippi River (Deutsch *et al*., 1973; Rango and Anderson, 1974; Morrison and White, 1976; see Smith, 1997). During later stages Satellite Pour l'Observation de la Terre (SPOT) multi spectral imagery were also used for flood delineation (Brouder, 1994; Oberstadler *et al.*, 1997; Sado *et al.*, 1997; see Sanyal and Lu, 2004). Radar imagery onboard satellites also has proved invaluable in mapping flood extent (Horritt, 2000; Schumann *et al*., 2007). The advantages of radar remote sensing over optical sensors are that it can penetrate through cloud cover, haze and dust since the microwave wavelengths that radar uses are not susceptible to atmospheric scattering that affects shorter optical wavelengths. This property allows detection of microwave energy under almost all weather conditions. Also, unlike optical sensors, data can be collected at any time of the day. Hess *et al*. (1995) used Synthetic Aperture Radar (SAR) data to study the inundation patterns on the Amazonian floodplain, Brazil. Pope *et al*. (1997) employed SIR-C SAR data to identify seasonal flooding cycles in marshes of the Yucatan Peninsula, Mexico. Lakshmi and Schaaf (2001) used data from the Special Sensor Microwave Imager (SSM/I) to analyze the 1993 summer flood event of Midwestern United States using satellite and ground data. In addition to capturing flood extents, flood extent maps derived from SAR sensors have been used to validate hydraulic models (Horritt *et al*., 2007; Hostache *et al*., 2009). However, limitations of the SAR include geometric and radiometric distortions that arise from inaccurate image calibration and data processing difficulties (Shumann *et al*., 2007; see Kahn *et al*., 2011). Apart from these medium resolution imageries, coarse resolution imageries like Moderate-resolution Imaging Spectroradiometer (MODIS) data (Islam *et al*., 2010; Kahn *et al*., 2011; Fayne *et al*., 2017) and Advanced Very High Resolution Radiometer Radiometer (AVHRR) data have been also found useful for floods of a regional dimension (Ali *et al.*, 1987; Islam *et al.*, 2001, 2002; see Sanyal and Lu., 2004).

The Landsat suite of satellites have been of popular use for researchers throughout its history due to its availability, relatively high spatial, temporal and spectral resolutions (16-day re-visit period, 30 m and 11 bands (Landsat 8), respectively), and its extensive global-scale archive dating back to 1972. No other satellite/suite has this combination of attributes, which makes Landsat imagery of particular value to the global community. Its value has been demonstrated in many scholarly work. Seasonal to interannual variations in stage and floodplain inundation area were mapped in the Amazon Basin (Sipple *et al*., 1992; Koblinsky *et al*., 1993; Hess *et al*., 1995; see Smith, 1997). Intermittently flooded areas in Kenya that are potential breeding grounds for mosquitoes that carry the dangerous Rift Valley Fever virus were mapped by Landsat Thematic Mapper ™ and airborne polarimeter data (Pope *et al*., 1992). In the Indian Subcontinent, Nagarajan *et al.* (1993) used Landsat images and aerial photographs over the Rapti River in India to identify areas vulnerable to channel migration and floods. Recently, using Landsat 7 – ETM+ data, Ho *et al*. (2010) mapped flood hazard risk in the vu gia-thu bon alluvial plain in central Vietnam.

The main goals of this study are to: (1) generate flood inundation maps from Landsat 8-operational Land Imager (OLI) data using five different classification techniques, (2) evaluate the performance of a terrain-based approach of identifying cloud-obscured water pixels, and (3) assess the accuracy of these techniques in capturing the flood extent by validating these techniques against manual digitization of flood extent.

STUDY AREA

This study focused on a flood event which happened along the lower portion of the Brazos River in Texas, USA during the week of May 26th to 31st, 2016 (Figure 1). The Brazos River, with a drainage basin of about 112,500 km^2, flows for more than 1900 km from its headwaters in the southern High Plains of New Mexico to its terminus at the Gulf of Mexico near Galveston, Texas (Vogel and Lopes, 2009). In the study area near Hempstead, the Brazos River is a perennial meandering river with an average gradient of 0.2 m/km and sinuosity of 1.8 (Waters and Nordt, 1994). The surrounding area itself is characterized by flat topography (greatest difference in elevation in the flooded area was found to be ~50 m) and low slope (0-5%). Climate in the study area is characterized as hot, humid summers and dry winters with high-peak streamflow events tending to occur in late spring (May, June) or early fall (September, October) (NCDC 2006; see Vogel and Lopes, 2009). Farming and ranching are major land uses in this area. Sixty to 70 percent of the land area is native grassland used for livestock grazing. The remaining 30 to 40 percent is used for growing crops such as wheat, cotton, and grain sorghum (Vogel and Lopes, 2009). The study site is located approximately 30 km above the United States Geological Survey (USGS) gage at Brazos River near Hempstead (ID: 08111500) on the main stem of the river.

[INSERT FIGURE 1 HERE][Figure 1. (A) Location of the study area in Texas, USA. (B) The location of the study domain on the Brazos River]

METHODOLOGY

Satellite Image preparation

For flood mapping using remotely sensed imagery, two sets of data are required. One set consisting of data acquired before (and as close as possible) to the flood event to make informed decisions about general conditions of the pre-flood environment, and the other acquired during or right after the occurrence of the flood. In this study, the Brazos River segment in the study site reached peak discharge of 4445.7 m^3/s at 3 p.m. on May 27th (recorded by USGS gage at Brazos River near Hempstead; ID: 08111500). The same gage also recorded total of 255.8 mm precipitation within 25 hours that resulted in the discharge.

Due to the 16-day overpass cycle of the Landsat 8 satellite, the availability dates for images of pre-flood data are from May 12th, April 26th, April 10th, and March 25th (and further back). The image acquired on March 25th 2016 was used for pre-food analysis as there was no cloud cover observed over the study site (path 26/row 39). For the during-flood image, the Landsat 8 image captured on May 28th at 12 p.m. (CDT) was used. This image was the closest available, to the day of peak discharge and had low cloud cover (<20 %). Although this was 21 hours after the peak discharge occurred, the stage height only decreased about 2.5% since the peak discharge (Figure 2), indicating that the river was receding slowly after peak stage conditions. Thus, it is rational to state that image from the May 28th 2016 captured the flood extent very close to its peak extent. The two images corresponding to the aforementioned dates (March 25th and May 28th) were downloaded from USGS Earth Explorer (United States Geological Survey Earth Explorer. Accessed July, 2016, http://earthexplorer.usgs.gov).

[INSERT FIGURE 2 HERE] [Figure 2. Stage hydrograph, rainfall hyetograph, time of peak discharge and date of image capture. Modified from Zhang *et al*., (2016)]

Erdas Imagine®- 2015 Image processing software (Hexagon Geospatial, Norcross, GA, USA) was used for image pre-processing and subsequent data manipulation of this study. Downloaded imagery were subject to Geometric and Radiometric corrections and were subset to cover only the study site, in order to prepare for image analysis of the flooded area.

Cloud cover correction

The existence of cloud cover/shadows is the most significant impediment for capturing the progress of floods during bad weather conditions (Lowry *et al.*, 1981; Rashid *et al.*, 1993; Melack *et al.*, 1994; see Sanyal and Lu, 2004). Cloud-free data acquisition for a single date is difficult and even in this study, although the cloud cover on the entire during-flood image was less than 20%, clouds and shadows were sporadically observed in the study domain (Figure 3).

[INSERT FIGURE 3 HERE] [Figure 3. Comparison of (A) Pre-flood and (B) During-flood imagery]

The following procedure was adopted to correct for cloud cover/shadow. Hereinafter this procedure will be identified as the 'DEM-based approach' used to classify cloud-obscured water pixels.

1) An infrared based false color composite (derived from band combination 5, 4, 3 for improved visualization of feature classes of interest) of the during-flood image was used to manually digitize (more details on the digitization process can be found under 'Reference flood generation') a flood extent polygon. The polygon was used to clip the flooded domain elevation data from a DEM (30 m resolution; 2.44 m absolute vertical accuracy expressed as the root mean square error (RMSE); downloaded from National Elevation Dataset. Accessed July, 2016, https://lta.cr.usgs.gov/NED).

2) Since the entire study region is relatively flat with minimal topographical variation (elevation beneath clouded areas especially varied by less than 50 ± 2.44 m, taking RMSE into consideration) and low slope, the pixel with the maximum elevation (hereinafter referred to as 'maximum elevation pixel') of the previously digitized flooded area was identified from the clipped DEM and used as the threshold pixel elevation to determine flooded pixels in cloud covered areas

3) The clouds were digitized from the false color composite into a new layer. Raster calculation tools were used to extract the pixels within cloud polygons that had elevations lower than the ‘maximum elevation pixel’. These pixels were classified as water and added to the digitized flood extent layer. These pixels will also be added to each classification output.

[INSERT FIGURE 4 HERE] [Figure 4. Flowchart of ‘cloud-water layer’ generation]

Reference flood generation

In order to have a reference flood to compare the classification techniques against, the flood water extent of the during-flood image was manually digitized. The digitization was done based on user knowledge, expertise and supplementary data sources (e.g. newspaper reports which included specific geolocations of the flood; these were used as reference points) of the Brazos flood. The digitization was performed using an infrared based false color composite of the during-flood image. A false color composite was used mainly because water features take extreme dark tones when viewed in this form and eases the task of delineating water pixels. In this delineation process, the ‘cloud-water layer’, with potential flooded areas located beneath clouds, formerly created using the ‘DEM-based approach’, was also merged to improve flood extent mapping. The digitized raster hereinafter will be referred to as the ‘reference flood’.

Floodwater classification

The following five feature classification techniques were employed on the flooded imagery to ascertain which performed the best in flood water pixel identification. With the exception of the Delta cue change detection technique, all other image analysis algorithms were performed on the during-flood image. Delta-cue utilized both the pre- and during-flood images.

(1) Supervised Classification based on the maximum likelihood classifier

Supervised Classification has been demonstrated to be a robust method to classify features of interest (Frazier and Page, 2000; Shalaby and Tateishi, 2007). The Supervised Classification technique is based on the idea that a user can select sample pixels in an image as representatives of a specific spectral signature class (end members; e.g. water). Subsequently, all the image pixels are classified based on the maximum likelihood that they are similar to one of the user-defined classes.

(2) Unsupervised Classification based on the K-means classification algorithm

Unsupervised classification is where the outcome of the classification processes (groupings of pixels with common characteristics) is based on automated analyses by the image analysis software. In this instance, the user does not provide sample pixels (training areas) for the software to gather information on spectral signatures. The user only specifies the desired number of output classes but otherwise does not aid in the classification process. However, it is important for the user to have knowledge of the area being classified when the groupings of pixels with common characteristics produced by the classification algorithm have to be related to actual features on the ground (such as water bodies, vegetated areas, and barren land, etc.). The K-means classification algorithm used in this study is based on partitioning *n* number of observations into *k* number of clusters in which each observation belongs to the cluster with the nearest mean, serving as a prototype of the cluster (Jenson, 2015). The study region was initially classified into 8 different classes and then consolidated into four classes by the user to represent earth-features (i.e. water, vegetation, bare soil, built up).

(3) Delta-cue change detection

This method is based on detection and analysis of changes between two images of the same area. The pre- and during-flood imagery were used to assess the change in water pixels between the two dates. A new layer was created using the 'new' water (water added to the study area as a result of the flood) that was found as a result of the change detection. This layer was subsequently clipped to the pre-flood image to generate the inundation map with 'total water' during the flooding period.

(4) Normalized Difference Water Index

The Normalized Difference Water Index (NDWI) (McFeeters, 1996; see Zha *et al*., 2003), is a spectral water index that utilizes the Green and Near Infrared (NIR) Bands of the satellite image for the delineation of open water. NDWI (1) magnifies the higher reflectance value of water in the green band, (2) diminishes the low reflectance value of water in the NIR band and, (3) makes use of the distinguished contrast between water and land of NIR band. The NDWI is calculated as:

$$NDWI = \frac{Green - NIR}{Green + NIR} \tag{1}$$

(5) Modified Normalized Difference Water Index

The NDWI values of urban land were found to be coincident with that of water in green band and NIR band. Xu (2006) proposed the use of the modified NDWI (MNDWI), where open water features are enhanced while efficiently eliminating built-up land noise and suppressing vegetation and soil noise. The MNDWI uses the Shortwave Infrared (SWIR; band 5) instead of the Near Infrared (band 4) of Landsat 8:

$$MNDWI = \frac{Grenn - SWIR}{Green + SWIR} \quad (2)$$

The intention of using MNDWI in this study region, where the built-up area in the region is minimal, was more so to suppress the vegetation and soil signatures than to eliminate built up noise.

The use of spectral indices involves identification of a threshold value to distinguish between water and non-water features (i.e. the minimum NDWI and MNDWI values that correspond to water). Since there were no prior studies done in this domain, experimentation was done with different threshold values to obtain the best match against the reference flood. It was found out that 0.2 (NDWI) and 0.1 (MNDWI) produced maps with the best fit (These values were also reported by Mcfeeters, (2013) and Wang *et al*., (2013) as general values to be used in data deficient regions)

Post processing and accuracy assessment

These classification outputs were post processed through a 3×3 high-pass kernel to accentuate the water features. A high pass kernel has the effect of highlighting boundaries between features (e.g., where water body meets the vegetated land), thus sharpening edges between water and non-water pixels to enhance the edges and boundaries between water features represented in the raster.

The following procedure was carried out in order to create flood maps for all five classification techniques, which also accounted for cloud-obscured flooding. All water pixels in the five raster outputs from the classifications and the cloud-water raster were reclassified as 1 and the non-water pixels as 0. Subsequently the cloud-water raster was merged into the five classification outputs to create cloud-water-corrected flood maps.

In order to assess the accuracy of the cloud-water corrected flood maps, an accuracy assessment was carried out. In this study, the Advanced Fitness Index (AFI) was used to compare classified imagery against the 'reference flood'. AFI was originally developed as an aerial statistic to compare observed inundation of satellite imagery to predicted inundation of hydraulic simulations by Bates and De Roo (2000). In this study, however, it was adapted to calculate the accuracies of classification techniques against the reference flood. The probability of a water pixel on a classified image of being an actual water pixel is calculated through this statistic. The inundated as well as non-inundated areas are taken into account in this index as intersections and unions of the flooded/non-flooded regions and calculated using:

$$\text{Advanced Fitness (\%)} = \frac{IA_{obs} \cap IA_{ref} + NIA_{obs} \cap NIA_{ref}}{A_{obs} \cup A_{ref}} \times 100 \quad (3)$$

where IA_{obs}/NIA_{ref} is inundated/non-inundated area from the classified imagery, IA_{ref}/NIA_{ref} is inundated/non-inundated area from the reference flood, and A_{obs}/A_{ref} is the entire calculated area from the satellite imagery/reference flood. For example, if the number of inundated pixels in a classified image intersect with 10 pixels at the reference flood layer is 10, the number of non-inundated pixels in the classified image intersect with 5 pixels in the reference flood layer, and the total number of pixels (inundated and non-inundated) in both the classified image and reference image is 30, then:

$$\text{Advanced Fitness (\%)} = \frac{10+5}{30} \times 100 = 50\% \quad (4)$$

The accuracy assessment was carried out separately for cloud-water-corrected maps, and for maps before cloud-water-correction (the direct outputs of classification techniques) to make inferences of the improvement of flood map raster due to use of the DEM based cloud correction approach.

RESULTS AND DISCUSSION

Figure 5 shows a comparison between the initially clouded regions in the during-flood image and the regions where water could be found beneath clouds, subsequent to the cloud water correction.

[INSERT FIGURE 5 HERE] [Figure 5. (A) clouded regions in the study site as shown on a true color image and (B) potential areas where water could be logged ('cloud-water layer') as identified through the DEM approach, superimposed on a true color image]

Raster math performed on the cloud-water layer indicates that 76.1% of the initially clouded regions were calculated as having water. This is a significant percentage of water that would not have been recognized by the classification techniques had the clouds been digitized off the original image (which would result as 'holes' in the raster) or left them as they were (which would result in clouds not being classified as water due to the different spectral signature).

The DEM-based approach used in this study, however, has limitations. It is only meant to be applied in areas with flat topography (maximum elevation difference in entire flooded area ~50 m) with a low slope gradient (0-5%). If for example, the study region's topography was undulating, there is a possibility of flood water getting accumulated in high lying plateaus, but not necessarily in low lying areas adjacent to them. Thus, if the concept of the 'maximum elevation pixel' was applied to the entire study region, the low-lying areas would also portray flooded conditions which might not be the case. Another important aspect to consider when using this approach is the slope of the study domain. Even if the gradient of the study region is moderate, even though the upper areas on the gradient are flooding, the lower areas might not be necessarily flooding, and the 'maximum elevation pixel' might render inaccurate results. Hence the reliable and quick usage of this method is limited to very low gradient floodplains. An approach that identifies local maximum-elevation values can alleviate this limitation. Cohen *et al.*, (2017) developed a floodwater depth estimation tool, based on the extraction of elevation vales for each boundary pixel of flood inundation domain. This allows for local estimation of floodwater elevation.

Figure 6 shows the reference flood and the inundation maps produced by the five different classification techniques. The cloud-water correction has been made to all six map outputs. (i.e. the cloud-water layer' has been merged into all the six maps). The inundation area of the reference flood was 55.1 km^2 with a maximum floodplain width of app. 10 km. The areas that were consistently not captured by the classification techniques are circled in red.

[INSERT FIGURE 6 HERE] [Figure 6. Reference Flood and Inundation maps of different classification techniques: (A) Reference, (B) Supervised, (C) Unsupervised, (D) Delta-cue, (E) NDWI and (F) MNDWI]

Table 1 illustrates the comparisons of the advanced fitness indices between the five classifications (with and without the cloud water corrections) and the reference flood. Improvements were noted in every classification technique (~ 17%) with the utilization of the cloud water correction approach. The best fitness for improved imagery was produced by supervised classification with an accuracy of 86.4% while unsupervised, MNDWI and NDWI closely followed and clustered together at 79.6%, 77.3% and 77.1%. Delta-cue change detection yielded the lowest accuracy with 70.1%.

[INSERT TABLE 1 HERE] [Table 1. Comparison of the advanced fitness indices of the five classification techniques to the reference flood. (Supervised: Supervised classification, Unsupervised: Unsupervised Classification, Delta-cue: Delta-cue change detection, NDWI: Normalized Difference Water Index, and MNDWI: Normalized Difference Water Index)]

It is interesting to note that although the reference flood was also created based on the same during-flood image that was used for classifications, the agreement of the classifications with the reference flood were not as high as expected. This may be attributed to the fact that when creating the reference flood, user knowledge and expertise was used to delineate water logged areas under tree canopies. If, for example, a vegetated marshy land with minimal topographical variations is surrounded with water, it is safe to assume that water would be present beneath the canopy. The classification techniques, on the other hand, cannot identify the under-canopy water in Landsat imagery given the distinct spectral signature of vegetation and its relatively course spatial resolution. Under-canopy water classification has been studied quite extensively (Adam *et al*., 2002; Ozesmi and Bauer, 2002) but with no robust solution. Two of the authors, (Cohen and Munasinghe) are currently developing a topography-based algorithm to address this problem as part of the U.S. Flood Inundation Map Repository project (http://sdml.ua.edu/usfimr). Another possible reason could be that debris accumulation or high sediment load in certain areas changed the floodwater spectral response resulting in it not being classified as water. However, since the reference flood was created not merely based on user expertise on identifying flooded areas on imagery, but also supplementary data sources such as geolocations of newspaper reports and bulletins, a discrepancy between the classifications and the reference flood was noted.

The supervised maximum-likelihood classification produced the best fitness of 86.4% with cloud correction, an improvement of 16.7 % from its direct classification output. This technique proved to be more sensitive than the other classification methods for detecting water bodies. This outcome is understandable in that, the sample pixels of flood water are selected based on user knowledge. Zhang *et al*. (2017) used this output for comparing two hydraulic models for the same study area. One might wonder why the spectral indices did not perform better than the supervised classification since water pixels extraction in these two methods is purely based on reflectance values, and intuitive thought would suggest that reflectance based feature class clustering might be more successful. However, it is of importance to understand that when selecting sample pixels to create 'signatures' to train the maximum likelihood classifier in supervised classification, the user creates samples representative of different types of floodwaters. The brightness values/tones of flood water can differ even on the same image as a function of water depth, turbidity, underlying land cover, and solar illumination. However, user expertise is used in this instance to take into account these different floodwaters.

Classification of floodwater based on spectral indices (NDWI and MNDWI) are purely based on reflectance values. There is, therefore, a much higher probability that a floodwater pixel might be categorized into a different feature class due to the fact that spectral indices are based on domain-wide threshold. The threshold that is set to differentiate between water and non-water features could, in some instances act to categorize more/less water pixels than actually present. There is no definitive method of knowing this threshold since its value is highly empirical.

The results of supervised classification are comparable in nature to that of Frazier and Page (2000), where Landsat Thematic Mapper (TM) imagery were used to map water bodies in the Wagga Wagga region in south eastern Australia. As per their findings, supervised classification of the water bodies yielded an overall accuracy of 97.4%. Overall accuracy in this instance is the ratio between the total number of correctly classified water pixels divided by the total number of test pixels. However, the producer's accuracy defined as the ratio between the numbers of pixels classified on an image to the number of pixels of that feature class in the area of interest in reality, achieved only 59.6%. In other words, this classification was able to locate all of the major water bodies but underestimated the number of water pixels present on the image. One of the major reasons for this could be the dense vegetation present in the study area hindering the identification of water present under the canopy. Shalaby and Tateishi, (2007) used supervised classification to great effect to map land cover changes in northwestern Egypt. The change in salt marsh land on Landsat Thematic Mapper (TM) and Enhanced Thematic Mapper (ETM+) yielded producer's and user's accuracies of 100%.

The accuracies of the two spectral indices in this study were satisfactory at 79.6% (MNDWI) and 77.3% (NDWI), an improvement of ~17% from its initial classification values. It has to be emphasized that the study region is highly vegetated and the results, hence, are better than expected. It is also noted that the MNDWI performed only marginally better than NDWI. We can infer that since there was no vast built-up area in the study region, the MNDWI's utility over the NDWI is limited. However, the marginally better percentage suggests that the performance of the combinations of Green and Shortwave Infrared bands suppressed the soil and vegetation features and better accentuated the water features.

Delta-cue change detection yielded the lowest classification accuracy of 70.1%. This also yielded the lowest classification accuracy even without the cloud-water-correction approach. Although 70.1% is an appreciable fitness, this method grieves from certain inherent problems that could have led to this lower accuracy. Change detection is based on quantifying change of a certain feature of interest between two images of the same area. Although the pre-flood image was selected to as close to the during-flood image in order to keep other environmental variables constant, differences in atmospheric conditions, illumination, soil moistures and phenological changes in vegetation could hinder the quantification of change of water pixels between the two dates (Deer 1995: see Lu *et al*., 2004). Especially, even though the dates are located two months apart, the aforementioned factors could result in floodwater inundated pixels to be classified as dry in the during-flood image, yielding under predicted flood extent.

CONCLUSION

This study compared five floodwater identification techniques for Landsat 8- OLI imagery for a flood event over the Brazos River (Texas). Supervised classification of floodwater areas yielded the best classification accuracy of 82.4%, while the other techniques (unsupervised classification, delta cue change detection, NDWI, MNDWI) yielded lower correspondence to the reference flood inundation map. We conclude that supervised classification, using the maximum likelihood classifier, would be the recommended option for future flood classifications. Supervised classification does, however, require the greatest degree of user input and expertise (identification of end-members) for each site. It is therefore more labor-intensive which may be a limiting factor for some applications that require a degree of automation (e.g. near-real-time flood inundation mapping).

A topography-based (DEM-based) approach for estimating flooding in pixels obscured by clouds was also presented. This was used successfully to identify flood water pixels beneath clouds. The approach increased the number of water pixels available for each classification and, in turn, improved the fitness with the reference flood. We recommend this DEM-based approach for future flood classification studies conducted in areas with relatively flat topography (elevation variability ~50 m in the flooded region) and minimal topographical gradient (0-5% slope).

Future research will include the development of a robust topographic/remote sensing based approach to identify water pixels beneath the vegetation canopy and the use of high spatial resolution satellite imagery and DEMs to assess efficiencies of classification algorithms. It is also envisioned to automate the cloud cover correction technique (when applicable to topographic region) and also automate the flood water classification algorithms to expedite this process.

ACKNOWLEDGEMENTS

The authors would like to thank Dr. David Maidment (University of Texas at Austin), Dr. Richard McDonald (USGS), Dr. Sarah Paskievicz (University of Alabama), Adnan Rajib (Purdue University) and Peirong Lin (University of Texas at Austin) for their generous support in this endeavor. Cohen and Munasinghe extend their appreciation to the University Corporation for Atmospheric Research (UCAR) and the NWC for their support via the COMET Program Cooperative Project Grant under Cooperative Agreement No. Z16-23487 with the National Oceanic and Atmospheric Administration (NOAA). Tsang and Huang would like to thank Dr. Yi-Leng Chen for his assistance to the workshop travel and application.

LITERATURE CITED

Adam, E., O. Mutanga, and D. Rugege, 2010. Multispectral and hyperspectral remote sensing for identification and mapping of wetland vegetation: a review. *Wetlands Ecology and Management*, 18(3), 281-296. DOI: 10.1007/s11273-009-9169-z

Bates, P. D., and A.P.J. De Roo, 2000. A simple raster-based model for flood inundation simulation. *Journal of hydrology*, 236(1), 54-77. DOI: 10.1016/S0022-1694(00)00278-X

Cohen, S., Brakenridge, G. R., Kettner, A., Bates, B., Nelson, J., McDonald, R., Huang, Y., Munasinghe, D., and J. Zhang, 2017. Estimating floodwater depths from flood inundation maps and topography. *Journal of the American Water Resources Association (JAWRA)*, 1-12. DOI: 10.1111/1752-1688.12609

Fayne, J., J Bolten, C Doyle, S Fuhrmann, M Rice, P Houser and V Lakshmi, 2017. Flood mapping in the Lower Mekong Basin using MODIS observations. *International Journal of Remote Sensing*, 38(6), 1737-1757. DOI: 10.1080/01431161.2017.1285503

Frazier, P. S., and K.J. Page, 2000. Water body detection and delineation with Landsat TM data. *Photogrammetric engineering and remote sensing*, 66(12), 1461-1468. DOI: 0099-1112I0OI6612-1461

Hess, L. L., J.M. Melack, S. Filoso, and Y. Wang, 1995. Delineation of inundated area and vegetation along the Amazon floodplain with the SIR-C synthetic aperture radar. *IEEE Transactions on Geoscience and Remote Sensing*, 33(4), 896-904. DOI: 10.1109/36.406675

Ho, L. T. K., M. Umitsu, and Y. Yamaguchi, 2010. Flood hazard mapping by satellite images and SRTM DEM in the Vu Gia–Thu Bon alluvial plain, Central Vietnam. *International archives of the photogrammetry, remote sensing and spatial information science*, 38(8), 275-280.

Horritt, M. S., 2000. Calibration of a two-dimensional finite element flood flow model using satellite radar imagery. *Water Resources Research*, 36(11), 3279-3291. DOI: 10.1029/2000WR900206

Horritt, M. S., G. Di Baldassarre, P.D. Bates, and A. Brath, 2007. Comparing the performance of a 2-D finite element and a 2-D finite volume model of floodplain inundation using airborne SAR imagery. *Hydrological Processes*, 21(20), 2745–2759. DOI: 10.1002/hyp.6486

Hostache, R., P. Matgen, G. Schumann, C. Puech, L. Hoffmann, and L. Pfister, 2009. Water level estimation and reduction of hydraulic model calibration uncertainties using satellite SAR images of floods. *IEEE Transactions on Geoscience and Remote Sensing* 47(2), 431-441. DOI: 10.1109/TGRS.2008.2008718

Huang, C., Y. Chen, and J. Wu, 2014. Mapping spatio-temporal flood inundation dynamics at large river basin scale using time-series flow data and MODIS imagery. *International Journal of Applied Earth Observation and Geoinformation*, 26, 350-362. DOI: 10.1016/j.jag.2013.09.002

Islam, A. S., S.K. Bala, and M.A. Haque, 2010. Flood inundation map of Bangladesh using MODIS time-series images. *Journal of Flood Risk Management*, 3(3), 210-222. DOI: DOI:10.1111/j.1753-318X.2010.01074.x

Jensen, J.R., 2015. Introductory Digital Image Processing: A remote sensing perspective, Prentice Hall, Upper Saddle River, NJ. ISBN-13: 978-0134058160

Joyce, K. E., S.E. Belliss, S.V. Samsonov, S.J. McNeill, P.J. Glassey, 2009. A review of the status of satellite remote sensing and image processing techniques for mapping natural hazards and disasters. *Progress in Physical Geography*, 33(2), 183-207. DOI: 10.1177/0309133309339563

Khan, S. I., Y. Hong, J. Wang, K.K. Yilmaz, J.J. Gourley, R.F. Adler, and D. Irwin, 2011. Satellite remote sensing and hydrologic modeling for flood inundation mapping in Lake Victoria basin: Implications for hydrologic prediction in ungauged basins. *IEEE Transactions on Geoscience and Remote Sensing*, 49(1), 85-95. DOI: 10.1109/TGRS.2010.2057513

Lakshmi, V and K Schaaf, 2001, Analysis of the 1993 Midwestern floods using satellite and ground data. *IEEE transactions on geoscience and remote sensing*, 39(8), pp. 1736-1743. DOI: 10.1109/36.942552

Lakshmi, V. (Ed.), 2016. Remote Sensing of Hydrological Extremes. Springer international publishing, Switzerland. ISBN 978-3-319-43744-6

Lu, D., P. Mausel, E. Brondizio, and E. Moran, 2004. Change detection techniques. *International journal of remote sensing*, 25(12), 2365-2401. DOI: 10.1080/0143116031000139863

McFeeters, S. K., 2013. Using the Normalized Difference Water Index (NDWI) within a geographic information system to detect swimming pools for mosquito abatement: a practical approach. *Remote Sensing*, 5(7), 3544-3561. DOI: 10.3390/rs5073544

Nagarajan, R., G.T. Marathe, and W.G. Collins, 1993. Technical note Identification of flood prone regions of Rapti River using temporal remotely-sensed data. *International Journal of Remote Sensing*, 14(7), 1297-1303. DOI: 10.1080/01431169308953957

Ozesmi, S. L., and M.E. Bauer, 2002. Satellite remote sensing of wetlands. *Wetlands ecology and management*, 10(5), 381-402. DOI: 10.1023/A:1020908432489

Pope, K. O., E.J. Sheffner, K.J. Linthicum, C.L. Bailey, T.M. Logan, E.S. Kasischke, and C.R. Roberts, 1992. Identification of central Kenyan Rift Valley fever virus vector habitats with Landsat TM and evaluation of their flooding status with airborne imaging radar. *Remote Sensing of Environment*, 40(3), 185-196. DOI: 10.1016/0034-4257(92)90002-2

Pope, K. O., E. Rejmankova, J.F. Paris, and R. Woodruff, 1997. Detecting seasonal flooding cycles in marshes of the Yucatan Peninsula with SIR-C polarimetric radar imagery. *Remote Sensing of environment*, 59(2), 157-166. DOI: 10.1016/S0034-4257(96)00151-4

Robertson, A. I., P. Bacon, and G. Heagney, 2001. The responses of floodplain primary production to flood frequency and timing. *Journal of Applied Ecology*, 38(1), 126-136.

Sanyal, J., and X.X. Lu, 2004. Application of remote sensing in flood management with special reference to monsoon Asia: a review. *Natural Hazards*, 33(2), 283-301. DOI: 10.1023/B:NHAZ.0000037035.65105.95

Shalaby, A., and R. Tateishi, 2007. Remote sensing and GIS for mapping and monitoring land cover and land-use changes in the Northwestern coastal zone of Egypt. *Applied Geography*, 27(1), 28-41. DOI: 10.1016/j.apgeog.2006.09.004

Smith, L. C., 1997. Satellite remote sensing of river inundation area, stage, and discharge: A review. *Hydrological processes*, 11(10), 1427-1439. DOI: 10.1002/(SICI)1099-1085(199708)11:10<1427::AID-HYP473>3.0.CO;2-S

Vogel, A. L., and V.L. Lopes, 2009. Impacts of water resources development on flow regimes in the Brazos River. *Environmental monitoring and assessment*, 157(1), 331-345. DOI: 10.1007/s10661-008-0538-5

Wang, Y., F. Huang, and Y. Wei, 2013. Water body extraction from LANDSAT ETM+ image using MNDWI and KT transformation. In *Geoinformatics (GEOINFORMATICS), 2013 21st International Conference on* (pp. 1-5). IEEE. DOI: 10.1109/Geoinformatics.2013.6626162

Waters, M. R., and L.C. Nordt, 1995. Late Quaternary floodplain history of the Brazos River in east-central Texas. *Quaternary Research*, 43(3), 311-319. DOI: 10.1006/qres.1995.1037

Xu, H., 2006. Modification of normalised difference water index (NDWI) to enhance open water features in remotely sensed imagery. *International journal of remote sensing*, 27(14), 3025-3033. DOI: 10.1080/01431160600589179

Zha, Y., J. Gao, and S. Ni, 2003. Use of normalized difference built-up index in automatically mapping urban areas from TM imagery. *International Journal of Remote Sensing*, 24(3), 583-594. DOI: 10.1080/01431160304987

Zhang, J., D. Munasinghe, and Y.F. Huang, 2016. Comparison of Flood Inundation Mapping 544 Techniques between Different Modeling Approaches and Satellite Imagery. In: *National 545 Water Center Innovators Program Summer Institute Report*, Maidment, D.R., A. Rajib, P. 546 Lin, and E.P. Clark (Editors). Consortium of Universities for the Advancement of 547 Hydrologic Science, Inc. Technical Report No. 13, 122 p. DOI: 10.4211/technical.20161019

Zhang, J., Huang, Y., Munasinghe, D.S.N., Fang, N., Tsang. Y., and S. Cohen, 2017. Comparative Analysis of Inundation Mapping Approaches for the 2016 Flood in the Brazos River, Texas. *Journal of the American Water Resources Association*. DOI: 10.1111/1752-1688.12623

Table 1. Comparison of the advanced fitness indices of the five classification techniques to the reference flood. (Supervised: Supervised classification, Unsupervised: Unsupervised Classification, Delta-cue: Delta-cue change detection, NDWI: Normalized Difference Water Index, and MNDWI: Normalized Difference Water Index)

Classification Technique	**Advance Fitness Index (%)** (Without Cloud-Water Correction)	**Advance Fitness Index (%)** (With Cloud-Water Correction)	**Improvement (%)**
Supervised	69.7	86.4	16.7
Unsupervised	63.1	79.6	16.5
Delta-Cue	52.8	70.1	17.3
NDWI	60.1	77.1	17.0
MNDWI	59.8	77.3	17.5

FIGURE CAPTIONS

Figure 1. (A) Location of the study area in Texas, USA. (B) The location of the study domain on the Brazos River

Figure 2. Stage hydrograph, rainfall hyetograph, time of peak discharge and date of image capture. Modified from Zhang *et al*., (2016)

Figure 3. Comparison of (A) Pre-flood and (B) During-flood imagery

Figure 4. Flowchart of ‘cloud-water layer’ generation

Figure 5. (A) clouded regions in the study site as shown on a true color image and (B) potential areas where water could be logged (‘cloud-water layer’) as identified through the DEM approach, superimposed on a true color image

Figure 6. Reference Flood and Inundation maps of different classification techniques: (A) Reference, (B) Supervised, (C) Unsupervised, (D) Delta-cue, (E) NDWI and (F) MNDWI

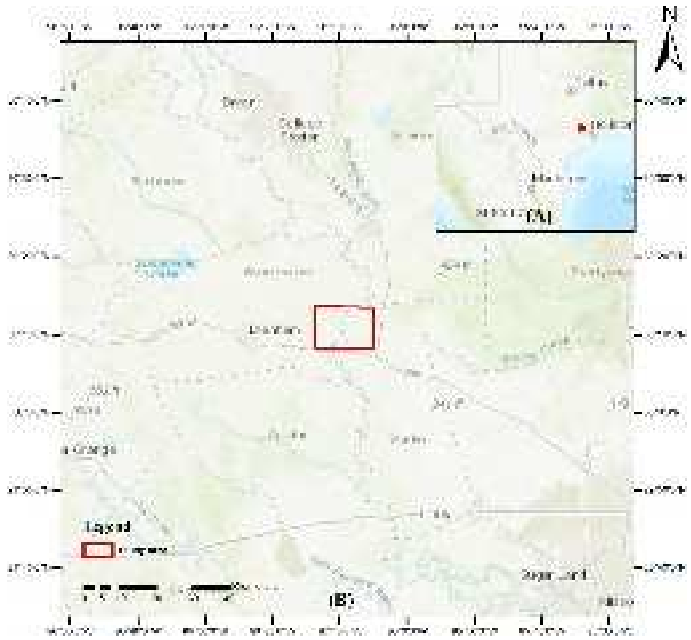

jawra_12626-17-0042_f1.tif

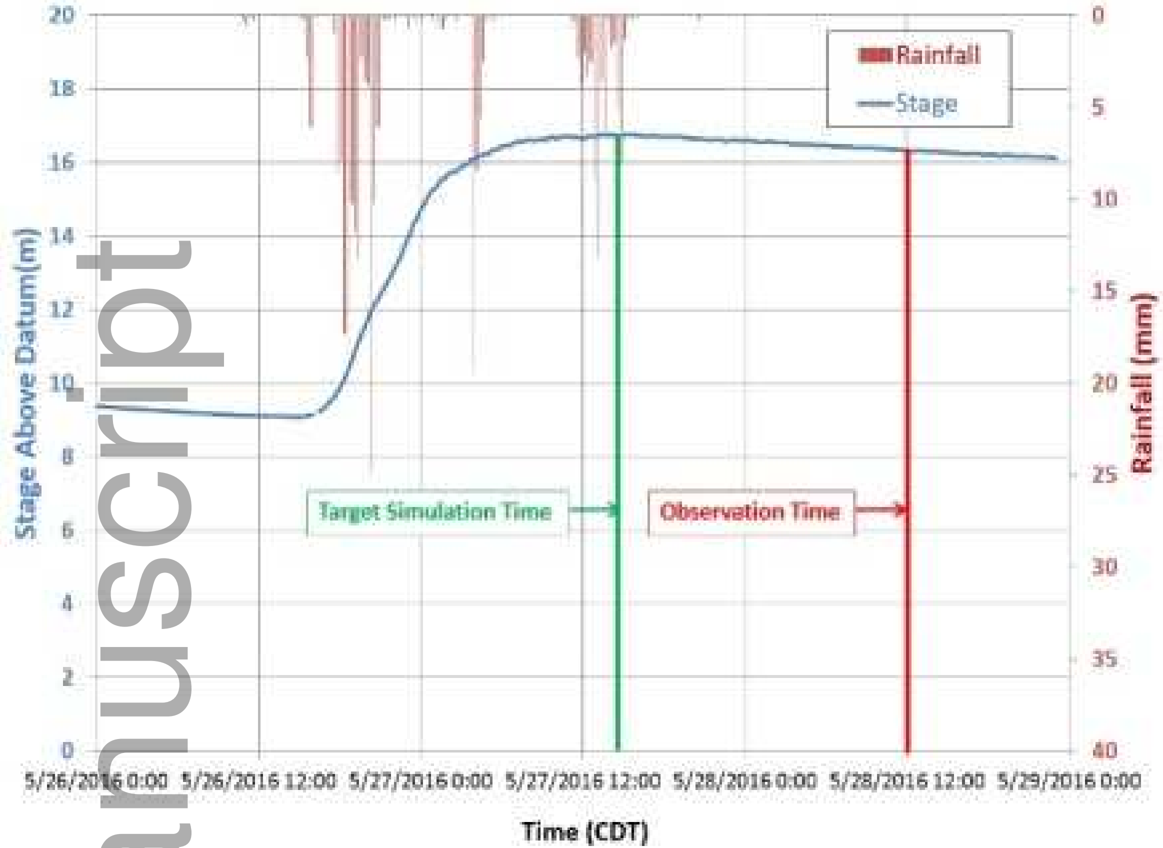

jawra_12626-17-0042_f2.tif

jawra_12626-17-0042_f3.tif

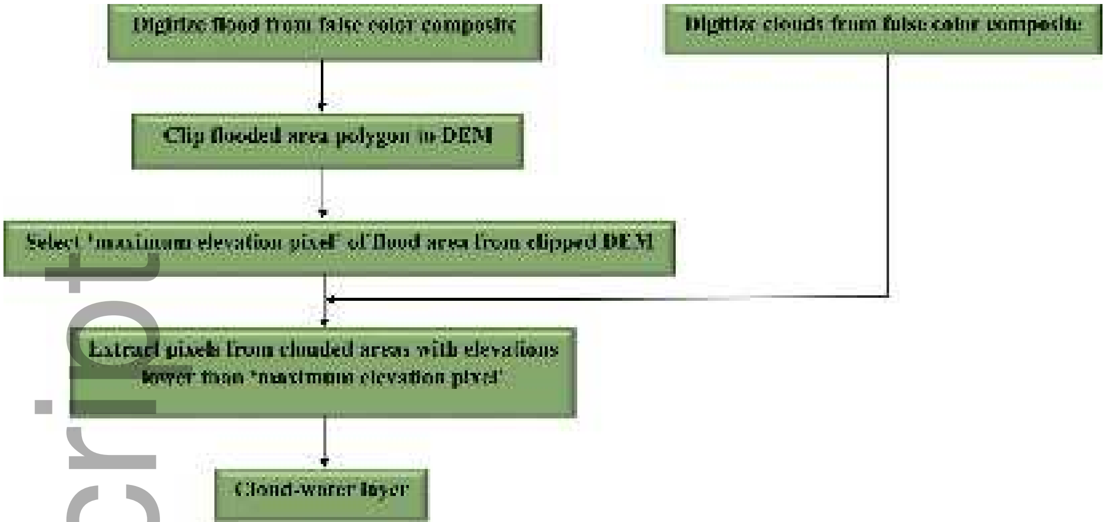

jawra_12626-17-0042_f4.tif

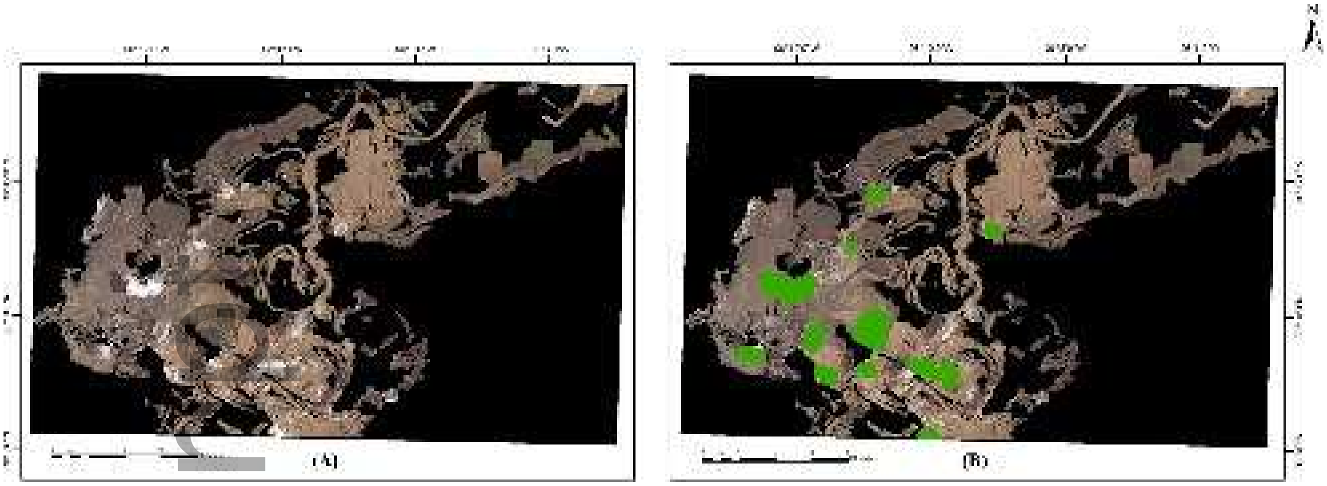

jawra_12626-17-0042_f5.tif

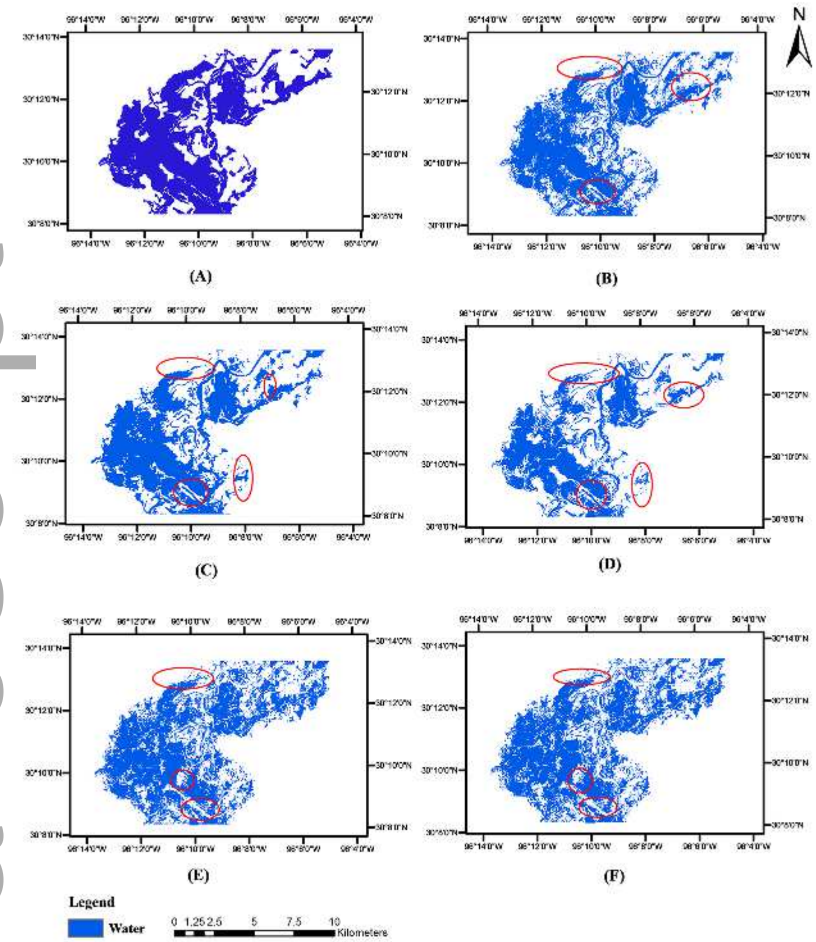

jawra_12626-17-0042_f6.tif